Eur. Phys. J. Plus (2023) 138:692
https://doi.org/10.1140/epjp/s13360-023-04319-0

THE EUROPEAN PHYSICAL JOURNAL PLUS

Regular Article

# Radiological characterization for the disposal of a decommissioned LHC external beam dump at CERN

**Angelo Infantino**[a], **Richard William Harbron, Renaud Mouret, Philippe Bertreix, Ana-Paula Bernardes, Luca Bruno, Marco Calviani, Gerald Dumont, Safouane El-Idrissi, Matteo Magistris, Nabil Menaa, Chris Theis, Christophe Tromel, Heinz Vincke**

European Organization for Nuclear Research (CERN), Esplanade des Particules 1, 1217, Meyrin Geneva, Switzerland

Received: 27 April 2023 / Accepted: 25 July 2023


**Abstract** During the last Long Shutdown, a scheduled maintenance period between physics runs, the two Large Hadron Collider (LHC) beam dumps were replaced with upgraded spares modules. It was then decided to conduct an in-house autopsy and a post-irradiation examination of the removed dumps to extract information essential for the 3rd LHC physics run and to aid the design of new generations of beam dumps able to cope with future upgrades of the LHC. The need for a postmortem analysis of the dump cores opened the opportunity to combine the autopsy with processes required for the disposal of the dumps as radioactive waste at a dedicated disposal facility in France. This had a direct impact in terms of overall optimization of the interventions (postmortem analysis and prepackaging) to be performed on the dump as well as in terms of minimizing of the radiological risk (ALARA), by reducing the exposure of the personnel by combining two interventions in one. The characterization of the dump as radioactive waste was performed by means of state-of-the-art Monte Carlo and analytical techniques verified experimentally via a series of dedicated radiochemical (using liquid scintillation) analyses, conducted in-house and in external specialized laboratories. Based on these results, the dumps will be disposed of as intermediate–medium-level (FMA-VC) waste at the ANDRA CSA repository in France.

## 1 Introduction

The Large Hadron Collider (LHC) at CERN is the world's largest and most powerful particle accelerator, presently allowing proton–proton collision at $\sqrt{s} = 13.6$ TeV center of mass. The LHC consists of a 27-km ring of superconducting magnets, about 100 m beneath surface, at the border between Switzerland and France. Inside the accelerator, two high-energy particle beams (protons or heavy ions) travel in opposite directions, in separate beam pipes, before they collide at dedicated experimental points. The LHC has 8 access points corresponding to the so-called Long Straight Sections (as opposed to the curved part of the tunnel infrastructure, i.e., the arc) which serve as experimental or utility insertion regions. There are two high-luminosity experimental insertions located next to the experiments at Point 1 (ATLAS) and 5 (CMS) and two additional experimental insertions next to the experiments at Point 2 (ALICE) and Point 8 (LHCb), which also contain the injection systems. The beams only cross at these four locations and are focused onto the interaction point (IP) by superconducting low-beta triplets (quadrupoles). Points 3 and 7 are the momentum and beta-cleaning insertions, respectively. Point 4 hosts the RF system, while Point 6 contains the beam dumping system [1], which is the subject of this publication. Two LHC external dumps, known in CERN jargon as "Target Dump External" (TDE), are used (one for each circulating beam) and are essential devices for the accelerator operation. The two TDEs absorb the energy of the two counter rotating beams, including abnormal operation conditions (e.g., asynchronous beam dump). They are installed in two dedicated underground caverns (conventionally called UD62/UD68) located ∼750 m downstream from interaction point 6 (IP6). Each TDE (Fig. 1) is made of multiple blocks of graphite with different densities: 1710 × 2 mm thick sheets of low-density graphite (Sigraflex®1.1–1.2 g/cm$^3$, LDG) and 6 blocks (× 700 mm in diameter and length) of high-density graphite (Sigrafine® ∼1.73–1.77 g/cm$^3$, HDG). The graphite is contained in a 8520-mm-long and 722-mm-diameter duplex stainless steel vessel (318LN, also known as URANUS® 45), filled with $N_2$. The full TDE assembly is surrounded by ∼ 900 tons of iron shielding blocks which have been constructed using decommissioned ISR (intersecting storage rings) dipole yokes, partially filled with concrete [1]. The shielding

Radiological characterization for the disposal of a decommissioned LHC external beam dump at CERN.

[a] e-mail: angelo.infantino@cern.ch (corresponding author)

Published online: 08 August 2023

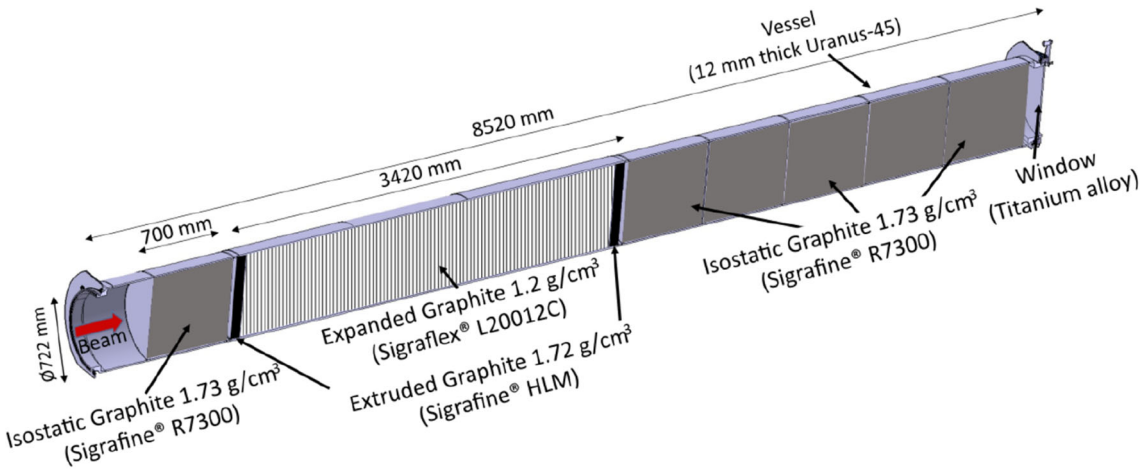


**Fig. 1** Schematics of the LHC beam dump core (TDE) [2]

aims to reduce the residual radiation levels during interventions in the UD caverns. The two dumps are owned and maintained by CERN Sources, Targets and Interactions Group (SY-STI).

During the last LHC physics period (Run 2, 2015–2018) several problems, which are described in depth by Maestre et al. [2], arose, related to excessive vibrations of the TDE and leakage of $N_2$. These challenges led to a modification of the TDE layout by replacing the two operational dumps with upgraded spares modules. Therefore, it was decided to conduct an in-house autopsy (i.e., to cut the TDE to inspect the graphite blocks) and post-irradiation examination (PIE) of the extracted TDE to obtain information essential for Run 3 operations (2022–2025), the production of new spare dumps and support the design of a new generation of dumps able to cope with the future high-luminosity LHC (HL-LHC) upgrade (up to 680 MJ of total stored beam energy [3]). The two operational TDEs used in Run 1 and Run 2 were extracted during the so-called Long Shutdown 2 or LS2 (2019–2021), a scheduled LHC maintenance period between Run 2 and Run 3 physics operations.

The TDE autopsy required several activities to be performed in high-radiation environment posing significant radiation protection (RP) challenges [4], due to the high residual activation of the TDE assembly (up to almost 10 mSv/h in contact after 1 year of cool down). The RP aspects related to preparation, optimization and execution of the TDE autopsy are discussed in a dedicated publication [5]. To ensure high safety standards and to respect the ALARA (as low as reasonably achievable) principle, these challenges were addressed by using state-of-the-art Monte Carlo techniques to predict the residual ambient dose equivalent rate and radionuclide inventory at different stages of the intervention. The CERN Radiation Protection group (HSE-RP) makes extensive use of the FLUKA [6–8] and ActiWiz [9] codes to produce accurate estimates of radionuclide inventories and associated activities. Ad hoc FLUKA benchmarks are reported in a number of publications such as [6–8] concerning FLUKA capabilities and nuclear models, and [10–13] concerning radiation protection-related topics (secondary emission yield, activation, deep shielding calculations and more). With regard to nuclear libraries, FLUKA cross sections are based on the hadronic nuclear models described in [7, 8]. Neutrons below 20 MeV are treated, by default, via a multi-group algorithm for which available neutron cross section evaluated data sets (ENDF, JENDL, JEFF) are used, as explained in [8]. ActiWiz makes use of the same FLUKA libraries concerning hadrons and high-energy neutrons (above 20 MeV). In addition, JEFF 3.3 are used for neutrons below 20 MeV, as reported in [9]. In this paper, FLUKA results will be compared with radiological measurements (e.g., H-3 specific activity). These comparisons were performed for cross-validation of the simulation setup rather than a benchmark of the FLUKA nuclear models, which is out of the scope of this paper.

The need for a postmortem analysis of the TDE core opened the opportunity to combine the autopsy with procedures required for radioactive waste (RW) conditioning/packaging. This had a direct impact in terms of optimization of the interventions to be performed on the TDE, namely the autopsy, post-irradiation examination, characterization and disposal. This led to significantly reduce future costs for materials, services and resources allocated for the autopsy and packaging (e.g., combined worksite, cutting sequence and tools optimized also in view of the packaging, remote handling and robotic tools and more) as well as the minimization of the radiological risk (i.e., optimization, ALARA) by reducing the exposure of the personnel combining two interventions in one. While a detailed overview of the radiation protection studies conducted in the context of the preparation of the autopsy is reported in Infantino et al. [5], this paper aims to report on the characterization of the LHC dumps as radioactive waste.

While the activation of the graphite in graphite-moderated nuclear reactors has been discussed in scientific literature [14–16], previously published information on the radiological characteristics of a beam dump subjected to a 6.5 TeV/*c* proton beam is nonexistent. Indeed, the LHC beam dump is subjected to a unique radiation environment coming from the unique characteristics of CERN accelerator complex. As it will discussed in paper, the LHC beam dump is subjected to a radiation environment given from the interaction of the 6.5 TeV primary protons with the graphite core as well as from high-energy secondary particles (neutrons, charged

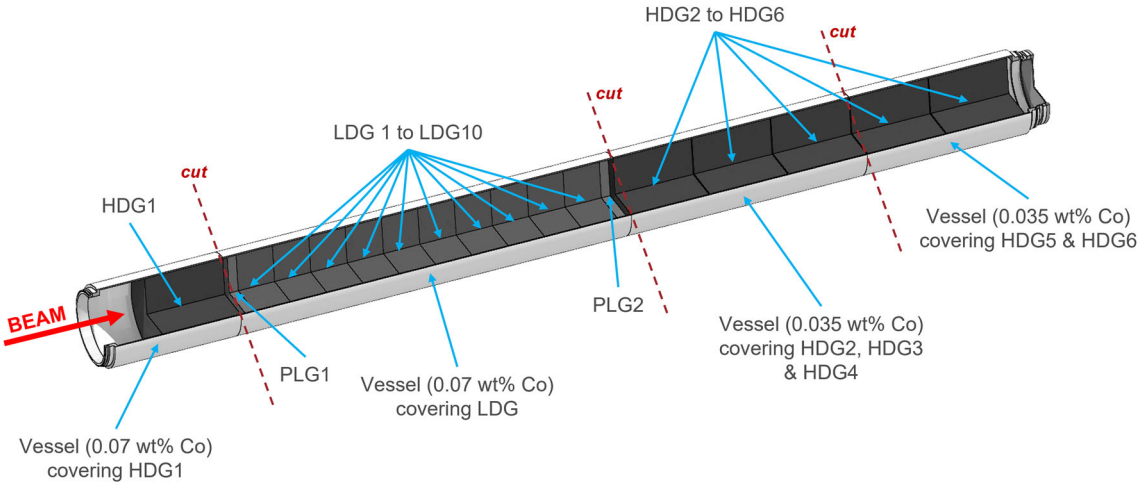


**Fig. 2** FLUKA model of the LHC beam dump core (TDE). The different regions represent the high-/low-density graphite blocks and the stainless steel vessel. The three dashed lines represent the main transverse cuts performed during the TDE autopsy

pions and more) coming from the hadron and electromagnetic particle shower developed within dump: This radiation environment is significantly different from the one it can be found in graphite-moderated nuclear reactors, and therefore, it cannot directly compared with, so that a number of innovative approaches were therefore required in order to estimate the activities of various radionuclides and plan the disposal of the LHC beam dump as radioactive waste. This paper describes our experiences, including (1) the use of Monte Carlo techniques and radiological measurements to estimate activities, (2) the analysis of these activities in the context of the various limits imposed by waste storage facilities, (3) the determination of optimum packaging for waste storage and (4) transport considerations.

## 2 Estimate of the LHC TDE activation by FLUKA simulations

Simulations were performed using the Monte Carlo code FLUKA (FLUKA.CERN Version 4-2.2) to characterize the TDE in terms of the radionuclide inventory produced in all the different parts of the LHC dump core. A detailed FLUKA model of the TDE core, the surrounding iron and concrete shielding and the UD cavern infrastructure was used to produce estimates relevant for the preparation of the TDE autopsy, as described in our publication [5]. Compared to the model reported by Infantino et al. [5], the model of the dump core was further improved in terms of material composition (e.g., different cobalt content in the 318LN steel to account for different batches composing the vessel) and geometry, by subdividing the core into different regions in order to match the autopsy cutting sequence, as performed. Figure 2 shows the new FLUKA model of the TDE core, as used in the present work.

As described above, the TDE core is made of different blocks of high- and low-density graphite (respectively, HDG1 to HDG6 and LDG). The LDG section was further subdivided into 10 regions (LGD1 to LDG10) to match the autopsy cutting sequence performed in February 2022. PLG1 and PLG2 (PLG meaning polycrystalline graphite) represent two blocks of extruded graphite. All the graphite blocks are enclosed in a 318LN steel vessel. The chemical compositions of the graphite and the steel vessel were modeled based on a combination of in-situ measurements (specifically regarding cobalt content in steel), discussion with TDE experts at CERN (SY-STI) and assumptions from comparing simulations with experimental RP surveys [5]. In particular, impurities were included in both the graphite and the vessel. The chemical composition of the graphite used in our simulations is, in weight fraction: Al 1.79E–03, Ba 4.50E–05, Ca 8.96E–04, C 9.80E–01, Cr 1.34E–04, Co 9.00E–06, Cu 1.80E–05, Fe 2.69E–03, Pb 4.50E–05, Mg 8.96E–04, Mn 9.00E–05, Mo 4.50E–05, Ni 4.50E–05, K 8.96E–04, Si 1.16E–02, Na, 4.48E–04, Sn 1.80E–05, Ti 2.69E–04, W 1.80E–05. A cobalt (Co) content between 0.035 wt% (percentage weight fraction) and 0.07 wt% was used in different sections of the steel jacket (Fig. 2): This difference is based on measurements of the Co content as well as of the residual dose rate from the vessel. The chemical composition of the stainless steel 318LN used in our simulations is, in weight fraction: C 2.20E–04, Cr 2.25E–01, Co 7.00E–04 (3.50E–04), Fe 6.69E–01, Mn 1.49E–02, Mo 3.12E–02, Ni 5.34E–02, N 1.70E–03, P 2.30E–04, Si 4.50E–03, S 2.00E–05.

The primary 6.5 TeV/$c$ proton beam was handled by a dedicated source routine which generates a characteristic sweeping path in the TDE core, as shown in [5]. The routine samples the $x$ and $y$ coordinates, as well as the $p_x$ and $p_y$ momentum, from a dedicated trajectory file. Electromagnetic (EM) production and transport thresholds for electrons and positrons were set to 100 keV, while 10 keV was set for photons. All other particle transport thresholds were set to 100 keV, except for neutrons, for which 0.01 meV was set. Photonuclear interactions were explicitly enabled: A variance reduction technique (biasing) was applied to the graphite (low and high density) and the steel vessel to increase artificially the frequency of photonuclear interactions. The operation of the TDE is quite complex due to the different conditions that trigger the dump of the primary beam (end of a fill, emergency stop, failure

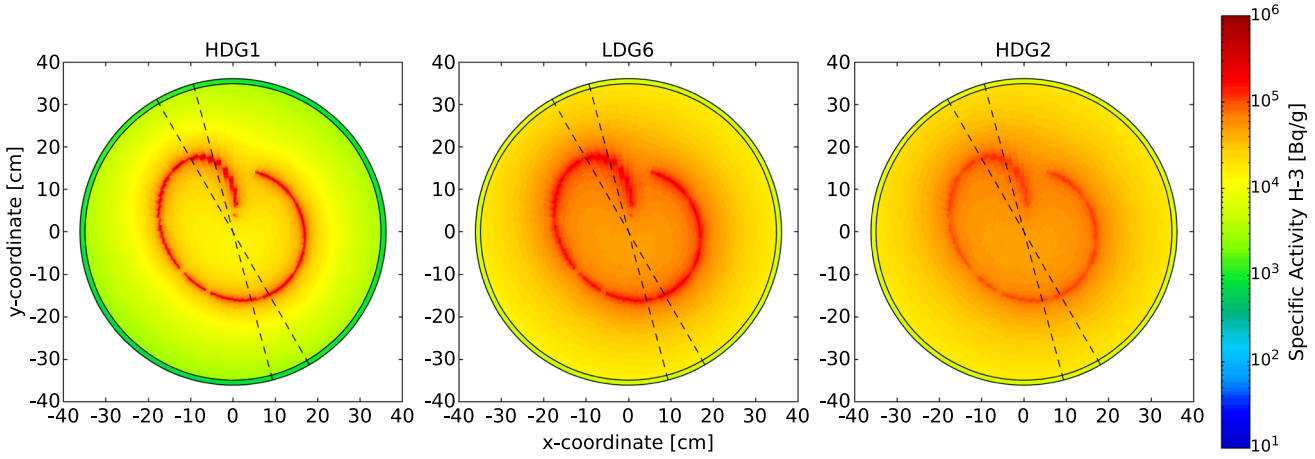


**Fig. 3** Specific activity H-3 over different sections of high-/low-density graphite (1724 days irradiation, $\sim 3 \times 10^{17}$ cumulative protons, 1245 days cool down). Circular crowns (dashed lines) highlight the areas used to produce the longitudinal plot

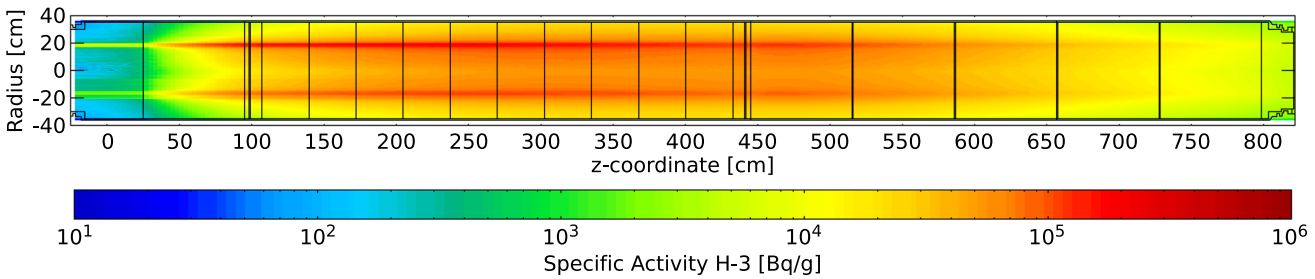


**Fig. 4** Specific activity H-3 over the TDE longitudinal axis (1724 days irradiation, $\sim 3 \times 10^{17}$ cumulative protons, 1245 days cool down). Average over $105° \leq \phi \leq 120°$ and $285° \leq \phi \leq 300°$ from positive $x$-axis

modes) and beam intensity (charges) extracted onto the core. A dedicated irradiation profile [5] was created in order to reproduce the operation during Run 1 and Run 2, based on the data available in the CERN Accelerator Logging Service [17]. A cumulative irradiation time of 1724 days and a total cumulative beam load of $\sim 3 \times 10^{17}$ protons were simulated.

FLUKA was used to score the $n$, $p$, $\gamma$, $\pi^+$ and $\pi^-$ fluence distribution in energy in each of the main components of the TDE core, accordingly to Fig. 2. These fluences were then incorporated into the analytical code ActiWiz Creator [9] to estimate the radionuclide inventory in the different parts of the TDE, based on the irradiation profile (i.e., the number of primary protons dumped during Run 1 and Run 2 operations) and the material composition.

In addition, the production yield of key radionuclides such as H-3, Co-60, Mn-54 and Fe-55 was estimated based on fluence conversion coefficients (FCC) [18]. The FCC method allowed to use ad hoc fluence-to-specific activity conversion coefficients generated considered the material composition of the different TDE components, the irradiation profile and a suitable cool down time. These coefficients were applied runtime to FLUKA, via a dedicated user routine, to generate 3D maps of the spatial distribution of the above-mentioned radionuclides. In particular, the coefficients were applied to cylindrical R-$\phi$-Z meshes covering the entire radius/length of the TDE core, with steps of 5 degree over $\phi$ (azimuthal angle around the longitudinal z-axis).

Figures 3, 4, 5, 6, 7, 8, 9 and 10 show the spatial distribution of the specific activity for H-3, Co-60, Mn-54 and Fe-55 within the TDE core, 1245 days of cooling time from the end of Run 2 operations. The cool down applied to the maps is relative to the day of the analysis of dedicated samples extracted from the TDE core, as will be discussed in Sect. 3. The cross sections showed in the plots (HDG1, LGD6 and HDG2) are also related to specific sampling locations. Figures 3 and 4 show how the H-3 distribution is mainly due to high-energy spallation reactions in the graphite matrix. Indeed, the activation follows the primary beam pattern. Conversely, Co-60, Mn-54 and Fe-55 (Figs. 5, 6, 7, 8, 9, 10) are mainly produced in the steel matrix (most external cylinder in the plots) by spallation and neutron capture reactions, while their production in the graphite matrix is at least one order of magnitude lower.

## 3 Radioactive waste classification

As part of a tripartite agreement between CERN and its host states, radioactive waste produced at CERN is disposed of as very low-level waste, TFA (from French très faible activité), at the ANDRA repository in France or intermediate- and low-level waste,

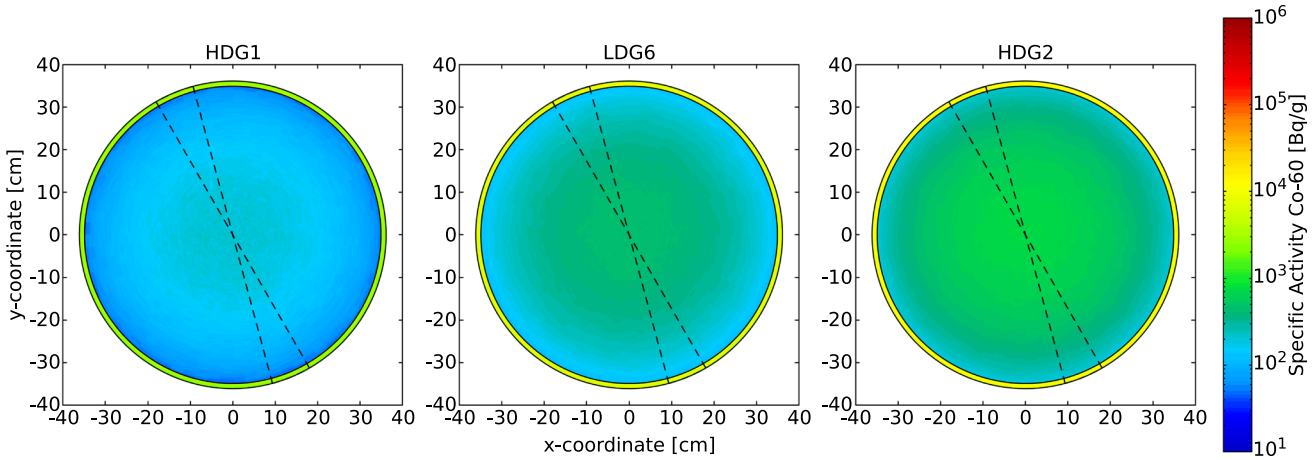


**Fig. 5** Specific activity Co-60 over different sections of high-/low-density graphite (1724 days irradiation, $\sim 3 \times 10^{17}$ cumulative protons, 1245 days cool down). Circular crowns (dashed lines) highlight the areas used to produce the longitudinal plot

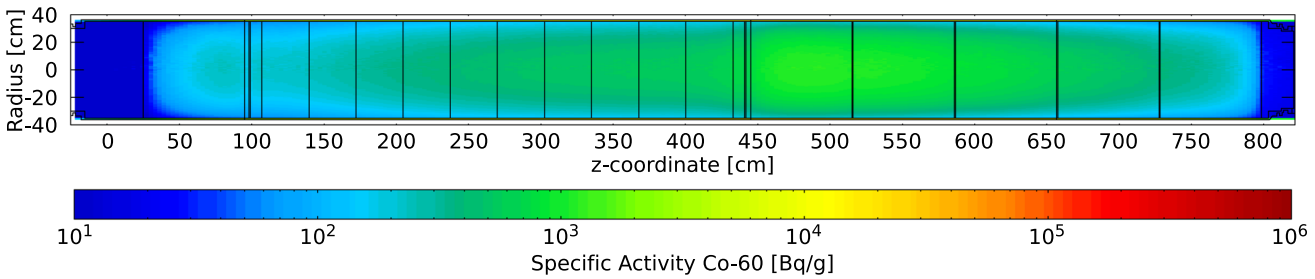


**Fig. 6** Specific activity Co-60 over the TDE longitudinal axis (1724 days irradiation, $\sim 3 \times 10^{17}$ cumulative protons, 1245 days cool down). Average over $105° \leq \phi \leq 120°$ and $285° \leq \phi \leq 300°$ from positive $x$-axis

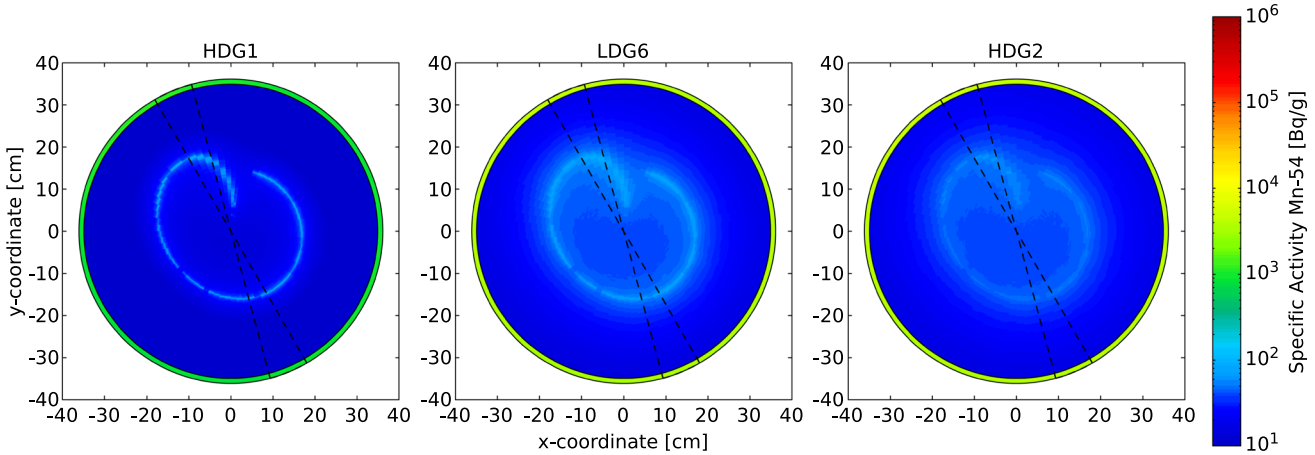


**Fig. 7** Specific activity Mn-54 over different sections of high-/low-density graphite (1724 days irradiation, $\sim 3 \times 10^{17}$ cumulative protons, 1245 days cool down). Circular crowns (dashed lines) highlight the areas used to produce the longitudinal plot

FMA (from French faible et moyenne activité), either at the ANDRA repository or in Switzerland, depending on activity levels. For a waste package to be classified as TFA, the "IRAS" (from French "Indice Radiologique d'Acceptation en Stockage," or Radiological Storage Acceptance Index) figure, calculated using Eq. (1), must be below 10.

$$IRAS = \sum A_i / AL \tag{1}$$

(where $A_i$ is the activity of nuclide $i$ in Bq/g and $AL = 10^j$, where $j$ is the nuclide-specific TFA class number). Waste exceeding the TFA limit is considered a candidate for FMA-VC (short-lived, i.e., $t_{\frac{1}{2}} < 31$ years) waste for storage at the ANDRA repository if the activities of all individual nuclides are below their respective LMA ("Limites Maximales d'Acceptabilité," or Maximum Acceptability Limits) threshold [19] (Table 1). In addition, ANDRA FMA waste must be encapsulated in a concrete matrix if any

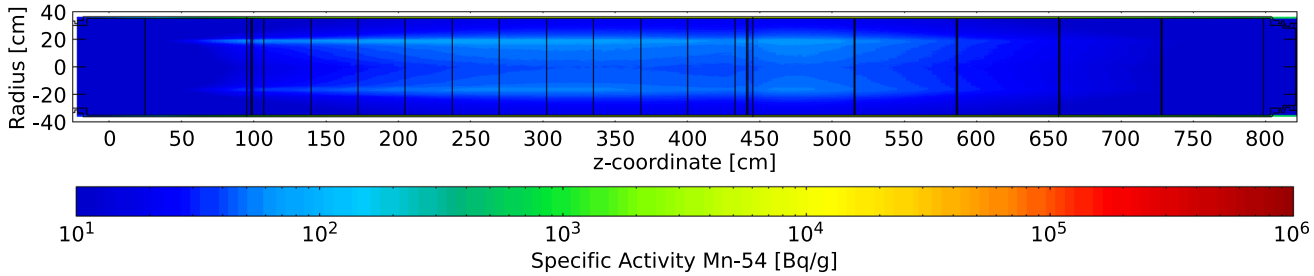


**Fig. 8** Specific activity Mn-54 over the TDE longitudinal axis (1724 days irradiation, $\sim 3 \times 10^{17}$ cumulative protons, 1245 days cool down). Average over $105° \leq \phi \leq 120°$ and $285° \leq \phi \leq 300°$ from positive $x$-axis

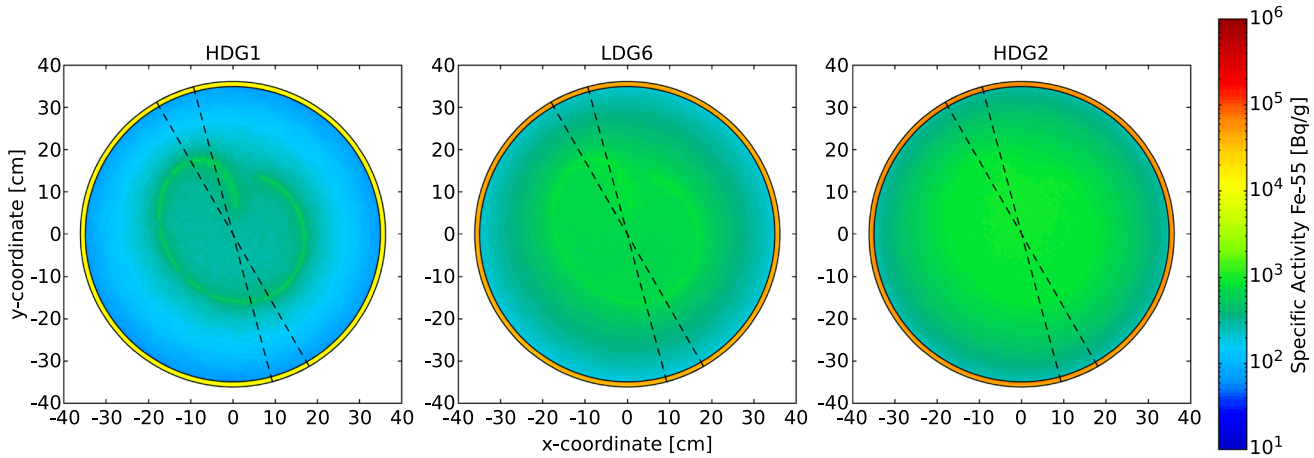


**Fig. 9** Specific activity Fe-55 over different sections of high-/low-density graphite (1724 days irradiation, $\sim 3 \times 10^{17}$ cumulative protons, 1245 days cool down). Circular crowns (dashed lines) highlight the areas used to produce the longitudinal plot

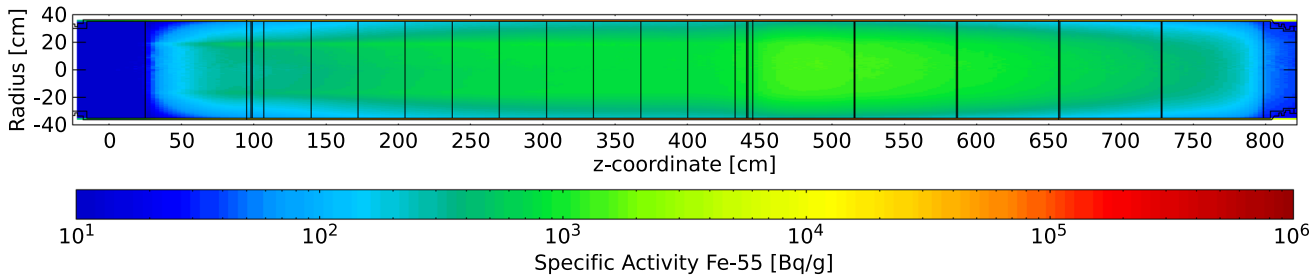


**Fig. 10** Specific activity Fe-55 over the TDE longitudinal axis (1724 days irradiation, $\sim 3 \times 10^{17}$ cumulative protons, 1245 days cool down). Average over $105° \leq \phi \leq 120°$ and $285° \leq \phi \leq 300°$ from positive $x$-axis

of the following four conditions are met: (1) the activity of *any* individual nuclide exceeds its respective encapsulation threshold (ET) [19] shown in Table 1, (2) the sum of activities for all $\beta$ and photon emitting nuclides in an item exceeds 37 kBq/g, (3) the activity of any $\alpha$-emitter with a half-life less than 31 years exceeds 3.7 kBq/g or (4) the sum of activities of all $\alpha$-emitters with half-lives $<$ 31 years exceeds 37 kBq/g. In addition, the sum of activities of $\alpha$-emitters must be below 185 Bq/g at 300 years. Finally, ANDRA imposes additional limits specific to H-3 and C-14, where 5 or 10 $m^3$ injection boxes are used (see section Sect. 5), the total H-3 and C-14 activities cannot exceed 50 and 20 GBq, respectively. Either must be declared if they exceed 5 GBq. If the requirements for disposal at the ANDRA repository are not met, the waste must be disposed of as FMA-MA (intermediate and low-level waste which does not fulfill the FMA-VC criteria) waste in Switzerland.

To determine the waste category of the LHC beam dump, the activities estimated using ActiWiz were compared to the limits for the waste categories described above. Calculations were performed for each region of the beam dump shown in Fig. 2 (four sections of the steel vessel, six high-density graphite sections and ten low-density graphite sections) using reported specific activities plus 2 $\sigma$ uncertainties. These uncertainties, which are well below 1% for most nuclides of interest, indicate statistical errors only (from both the nuclear data library and fluence spectra). Calculations were performed for activities representative of February 2022, when the beam dump autopsy took place.

**Table 1** ANDRA limits (in Bq/g)

| Nuclide | FMA-VC declaration | TFA | Encapsulation threshold | LMA |
|---|---|---|---|---|
| H-3 | 10 | 1000 | 7400 | 2.00E+05 |
| Be-10 | 0.0001 | 1000 | ∞ | 5.10E+03 |
| C-14 | 1 | 1000 | 3700 | 9.20E+04 |
| Na-22 | 1 | 10 | 21,000 | 1.30E+08 |
| Si-32 | 1 | 1000 | ∞ | ∞ |
| Cl-36 | 0.01 | 1000 | ∞ | 5.00E+00 |
| Ar-39 | 1 | 1000 | ∞ | ∞ |
| Ca-41 | 0.0001 | 1000 | ∞ | 3.00E+05 |
| Ti-44 | 1 | 10 | ∞ | ∞ |
| V-49 | 1 | 1000 | ∞ | ∞ |
| Mn-54 | 10 | 10 | 37,000 | 3.60E+08 |
| Fe-55 | 10 | 1000 | 37,000 | 6.10E+09 |
| Co-57 | 1 | 100 | ∞ | ∞ |
| Co-60 | 10 | 10 | 3700 | 1.30E+08 |
| Ni-59 | 0.1 | 1000 | 3700 | 1.10E+05 |
| Ni-63 | 1 | 1000 | 3700 | 3.20E+06 |
| Ge-68 | 1 | 10 | ∞ | ∞ |
| Nb-91 | 1 | 1000 | ∞ | ∞ |
| Nb-93 m | 10 | 1000 | ∞ | ∞ |
| Mo-93 | 0.001 | 1000 | ∞ | 3.80E+04 |
| Tc-99 | 0.01 | 1000 | ∞ | 4.40E+04 |
| Sn-121 m | 0.001 | 1000 | 37,000 | 3.70E+05 |
| Sb-125 | 1 | 10 | 37,000 | 5.10E+08 |
| Ba-133 | 1 | 10 | ∞ | ∞ |

Only nuclides exceeding the declaration threshold for FMA waste, estimated using Fluka/AW calculations, in the beam dump are shown
*AL* $10^j$ where j is the TFA class, *ET* encapsulation threshold, *LMA* maximum acceptability limits

Table 2 shows IRAS figures calculated using the activities estimated by ActiWiz for each region of the beam dump. IRAS figures easily exceed 10 for each region, meaning the beam dump could not be classified as TFA waste. The nuclides making the largest contributions to IRAS are H-3, Na-22 and Co-60 in the graphite regions, and Mn-54, Fe-55 and Co-60 in the steel vessel.

The LMA threshold is not reached by any nuclide, in any region of the beam dump. The most limiting nuclide is H-3, which does not exceed 35% of the LMA. For all other nuclides, the fraction of the LMA is well below 1%. This means the dump meets the requirements for disposal as medium-level (FMA) waste in France.

Table 2 also shows the sum of specific activities of $\beta$ and photon emitters in each region. This sum exceeds the ANDRA encapsulation threshold of 37 kBq/g in several regions of high- and low-density graphite, at February 2022. In addition, the nuclide-specific encapsulation threshold was exceeded by H-3 in all graphite regions. No other nuclides in the graphite region exceeded the encapsulation threshold. Activity levels in two regions of the steel vessel exceed 37 kBq/g, while nuclide-specific encapsulation thresholds were exceeded by Co-60 and Fe-55 in the vessel corresponding to the low-density graphite and high-density graphite regions 2-5.

### 3.1 H-3 activity

Table 2 shows total estimated H-3 activity for each region, calculated by multiplying specific activities by the respective region mass. Based on these figures, and depending on the number of graphite sections packaged together, the total H-3 activity could easily exceed 50 GBq, thus exceeding the limit set by ANDRA for a single 10 $m^3$ container. It is possible, however, that H-3 could diffuse out from the graphite matrix, meaning H-3 activities could be lower than predicted by the ActiWiz/FLUKA calculations. Theoretical calculations of outgassing are extremely sensitive to the structure of the graphite matrix, as well as to the temperature profile in the TDE core, and thus subject to large uncertainties. Given this, and given the cost implications of exceeding H-3 activity limits, the decision was made to perform radiochemical analysis (Jacobs Clean Energy Limited, Washington, UK) on samples of graphite to better estimate H-3 activity. This was performed by liquid scintillation counting following oxidation of all forms of H-3 by pyrolysis to titrated water. No specific radiochemical treatment or preconditioning was required during the sampling at CERN.

Samples were extracted from five longitudinal positions along the length of the beam dump, three representing the low-density graphite region and the remaining two representing high-density graphite regions 1 and 2. At each longitudinal position, four samples were extracted at different radial distances from the center (Fig. 11). The angular and longitudinal location of the samples was designed to be representative of the H-3 distribution predicted by FLUKA simulations, as shown in Figs. 3 and 8.

**Table 2** IRAS, beta-gamma ($\beta\gamma$) activity for all nuclides combined and total H-3 activity for each region of the dump

| Region | IRAS | $\beta\gamma$ activity (Bq/g) | Total H-3 (GBq) |
|---|---|---|---|
| HDG1 | 27 | 1.20E+04 | 5.5 |
| HDG2 | 164 | 6.50E+04 | 29.8 |
| HDG3 | 137 | 5.09E+04 | 23.3 |
| HDG4 | 96 | 3.37E+04 | 15.4 |
| HDG5 | 61 | 2.04E+04 | 9.3 |
| HDG6 | 34 | 1.14E+04 | 5.2 |
| LDG1 | 68 | 3.60E+04 | 4.9 |
| LDG2 | 85 | 4.51E+04 | 6.1 |
| LDG3 | 102 | 5.36E+04 | 7.2 |
| LDG4 | 116 | 6.06E+04 | 8.2 |
| LDG5 | 128 | 6.59E+04 | 8.9 |
| LDG6 | 136 | 6.91E+04 | 9.3 |
| LDG7 | 141 | 7.05E+04 | 9.5 |
| LDG8 | 142 | 7.02E+04 | 9.4 |
| LDG9 | 141 | 6.85E+04 | 9.2 |
| LDG10 | 140 | 6.59E+04 | 8.8 |
| Vessel HDG1 | 138 | 5.91E+03 | 0.1 |
| Vessel LDG | 1150 | 7.17E+04 | 4.7 |
| Vessel HDG2-4 | 938 | 2.52E+04 | 2.6 |
| Vessel HDG5-6 | 338 | 6.56E+04 | 0.8 |

Figures are based on activity levels at February 2022. Note: IRAS applies to whole waste packages, though figures for individual regions are shown here to illustrate the relative contribution to total IRAS

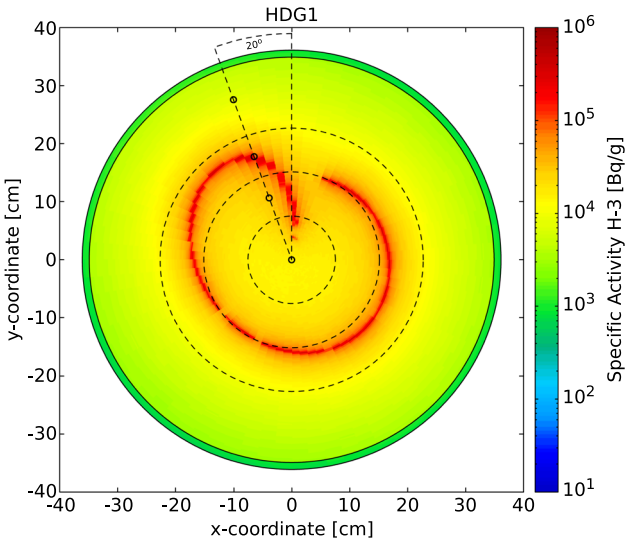


**Fig. 11** Overlay of the sampling points for first high-density graphite (HDG1) region. Bold circles (in scale) represent the samples while dashed (--) circles represent the graphite volumes used for weighting the results

For the high-density graphite, samples were obtained using a core drill bit, producing cylindrical samples of 10 mm diameter, 30 mm length and around 4 g mass. The samples have been extracted remotely by using an in-house robot developed by CERN's robotic team. For the low-density graphite, the core drill was considered unsuitable because the graphite disintegrated into fine fragments during testing, thus risking induced outgassing. Instead, a round metal punch was struck by a hammer to produce disks of 32 mm diameter and 2.5 mm thickness and 2 g mass.

Analysis was performed between 23–30 April 2022. H-3 activity in the regions represented by the samples was estimated by calculating a weighted average, accounting for the different graphite volumes represented by the different radial sampling points (Fig. 11).

Compared to the H-3 activities estimated using ActiWiz, the activities based on the sampling results are lower for LDG region 3, reasonably similar for LDG6 and higher for LDG8 (Table 3, LDG3, LDG6 and LDG8). Concerning the high-density graphite, the H-3 activity levels of the samples were much lower than respective figures obtained using ActiWiz (Table 3, HDG1 and HDG2). This suggests outgassing of H-3 has occurred from the high-density graphite but not the low-density graphite. Such differences likely reflect variation in the crystalline structure of the graphite between the two forms. We do not believe outgassing was induced

**Table 3** Total H-3 activities (GBq) based on sampling results compared to equivalent figures estimated using ActiWiz

| Region | Samples | Samples +2 $\sigma$ | ActiWiz +2 $\sigma$ | Combined |
|---|---|---|---|---|
| HDG1 | 2.3 | 2.6 | 5.5 | 2.6 |
| HDG2 | 5.5 | 6.1 | 29.8 | 6.1 |
| HDG3 | 4.3* | 4.8* | 23.3 | 4.8 |
| HDG4 | 2.9* | 3.2* | 15.4 | 3.2 |
| HDG5 | 1.7* | 1.9* | 9.3 | 1.9 |
| HDG6 | 1.0* | 1.1* | 5.2 | 1.1 |
| LDG1 | NA | NA | 4.9 | 6.9 |
| LDG2 | NA | NA | 6.1 | 8.6 |
| LDG3 | 4.3 | 4.8 | 7.2 | 10.2 |
| LDG4 | NA | NA | 8.2 | 11.6 |
| LDG5 | NA | NA | 8.9 | 12.5 |
| LDG6 | 9.0 | 10.1 | 9.3 | 13.2 |
| LDG7 | NA | NA | 9.5 | 13.4 |
| LDG8 | 11.9 | 13.3 | 9.4 | 13.3 |
| LDG9 | NA | NA | 9.2 | 13.0 |
| LDG10 | NA | NA | 8.8 | 12.5 |

Figures marked * are based on extrapolation from HDG2

by the sampling process itself, given the highly intact, unfragmented nature of the samples. The heat generated during drilling was substantially less than generated during beam dump aborts.

For the purposes of determining optimal packaging, the H-3 activity determined by sampling in HDG region 2 (HDG2) was extrapolated to regions 3–6 based on the activity ratio between these regions calculated using ActiWiz. Based on these calculations, the total activity of H-3 for the whole HDG region and the associated steel vessel is around 24 GBq. Thus, this region can be comfortably packaged together in a single 10 $m^3$ container without exceeding the 50 GBq limit. For the low-density graphite, activities estimated using ActiWiz were scaled by the ratio between sample and ActiWiz activities for LDG region 8 (where the ratio was the highest).

## 4 Transport of radioactive material

The transport of radioactive material on public roads is based on the agreement concerning the International Carriage of "Dangerous Goods by Road" (ADR [20]). This defines a certain number of rules that must be adhered to in order to transport radioactive goods safely on public roads. The application of ADR at CERN is defined and documented in a dedicated internal document, which defines the procedure for transporting radioactive goods between CERN's premises, covering intra- as well as inter-site transports.

Depending on the quantity of radioactivity transported, several safety measures are foreseen for the transport. As a general rule, the higher the activity levels are, the more stringent the transport constraints become, especially concerning the resistance of the transport package. In addition, dose rate limits also have to be taken into account to maintain external exposure within acceptable levels during transport.

Based on simulation results, the classifications for several transport scenarios have been estimated. These scenarios correspond to:

- Scenario 1a: the transport of the HDG and the HDG's steel vessel;
- Scenario 1b: the transport of the HDG, the HDG's steel vessel and all LDG parts;
- Scenario 2: the transport of the LDG parts;
- Scenario 3: the transport of the LDG's steel vessel.

Note that each transport is considered to be made in a single class 7 package/container.

For the purpose of transport classification, one can define the decision threshold for a specific classification as the sum over all the radionuclides, of the fractions of the activity over the corresponding transport limit. As a reminder, a certain transport classification can be used if the decision threshold is below 1.

Table 4 presents the transport classifications for the considered scenarios. Note that values in bold in the tables denote classifications that can be used for the transport, as they do not exceed unity.

Dose rate measurements [5] performed on the TDE did not show values exceeding 2 mSv/h at 30 cm from the dump, after more than 3 years cool down from the end of Run 2 operation.

**Table 4** Transport classifications for different scenarios

| | Decision threshold | | | |
|---|---|---|---|---|
| | Scenario 1a | Scenario 1b | Scenario 2 | Scenario 3 |
| Exempted total | 8.11E+04 | 8.68E+04 | 5.73E+03 | 8.92E+04 |
| Exempted specific | 1.67E+03 | 2.27E+03 | 5.99E+02 | 1.11E+03 |
| UN2910-excepted | 1.67E+01 | 2.06E+01 | 3.88E+00 | 1.73E+01 |
| UN2912–LSA-I | 5.56E+01 | 7.56E+01 | 2.00E+01 | 3.70E+01 |
| UN3321–LSA-II | **4.04E-04** | **6.86E-04** | **2.82E-04** | **2.36E-04** |
| UN3322–LSA-III | **2.02E-05** | **3.43E-05** | **1.41E-05** | **1.18E-05** |
| UN2915–Type A | **1.67E-02** | **2.06E-02** | **3.88E-03** | **1.73E-02** |

With respect to handling and transport, no major concerns have been identified for the four scenarios studied. Technical solutions exist for the packaging (ISO 20 or 40 feet containers IP2 certified, ISO 20 feet containers type A certified). For internal transport, CERN has its own class 7 certified packages. These package are generally not used for shipping of radioactive materials.

Regarding the internal transport of the LDG steel vessel (scenario 3), CERN owns an IP2 container for large materials. The inner dimensions of this container ($9.764 \times 1.400 \times 2.280$ m$^3$) allowed the successful transfer of the LDG steel vessel from CERN point 6 to the ISR facility on Meyrin site. Depending on the conditioning of the LDG steel vessel when it will be evacuated outside CERN, we may consider the rental of a 40 foot IP2 package. Particular attention should be paid to the verification of the dose rate at contact of the container (limited to 2 mSv/h).

Regarding scenarios 1a, 1b and 2, it is foreseen that the radioactive materials will be packed in a specific waste package (see Sect. 5). Taking into account the dimensions and the maximum weight of this waste package loaded ($3400 \times 1700 \times 1700$ m$^3$, 13.55 tons, scenario 1a and 1b) CERN's IP2 container for the internal transport of large material cannot be used for the transfer between CERN point 6 to the ISR facility on Meyrin site. In order to transfer the HDG region (including its respective steel vessel and possible LDG parts), CERN has only one option available, namely its own Type A 20 foot container. Thanks to the 15 cm thickness of concrete shielding provided by the waste package, the limits of 10 mSv/h at contact with the package and 2 mSv/h at contact with the Type A container are not expected to be exceeded. For the final elimination outside CERN, the rental of a 20 foot type A or IP2 package might be possible.

## 5 Radioactive waste prepackaging

As reported in the waste classification Sect. 3, the dump shall be classified as FMA waste, with the requirement that the waste be encapsulated. The most appropriate elimination pathway for this class of waste is the CSA (Centre de Stockage de l'Aube) in France. At the CSA, only standard storage containers are allowed. The container is in fact the first safety barrier implemented to meet the general safety objectives of containment and environmental protection. Considering the TDE dimensions, only two standard conditioning options are available for its storage at CSA while meeting specific ANDRA's specifications: an injectable container of 5 m$^3$ and an injectable container of 10 m$^3$. It is important to note that CERN will only precondition the dump (characterization, cutting of the dumps in appropriate pieces, preparation of the packages following ANDRA specifications). On the other hand, the final conditioning (e.g., filling the container with concrete) and storage of the radioactive waste package will be performed by ANDRA. While this work provides the methodology for the radiological characterization of the LHC beam dump as radioactive waste, the details of the final conditioning at the ANDRA CSA center are out of the scope of the present paper.

This type of package is accepted at the CSA for disposal in concrete-filled vaults (in French, "Ouvrage Betonné"). Two versions are available: simple and pre-concreted containers. For the TDE, it was decided to use a pre-concreted container with an inner layer of concrete of thickness 150 mm, ensuring both containment and radiological protection. The mortar used for the final injection must meet the ANDRA requirements in terms of mechanical and containment properties (gas permeability, compressive and tensile strength, water porosity, shrinkage, etc.). It is necessary to carry out an exhaustive set of technical tests to demonstrate that these requirements are met. To avoid any problem with this mortar, we decided to let ANDRA perform the injection themselves at the CSA.

In addition to the radiological limits detailed in Sect. 3, other criteria need to be respected in accordance with the ANDRA's specification:

- A list of forbidden waste is defined in ANDRA's specification. The TDE dump does not include this type of material.
- A list of waste accepted with restriction is defined in ANDRA's Specification. The TDE dump is only composed of nonreactive metal and graphite. These two materials are accepted without restriction.
- The injectable containers shall withstand with a maximum gross weight of 19 tons. The container that will be used passed all the necessary tests for a weight of 13.55 tons.

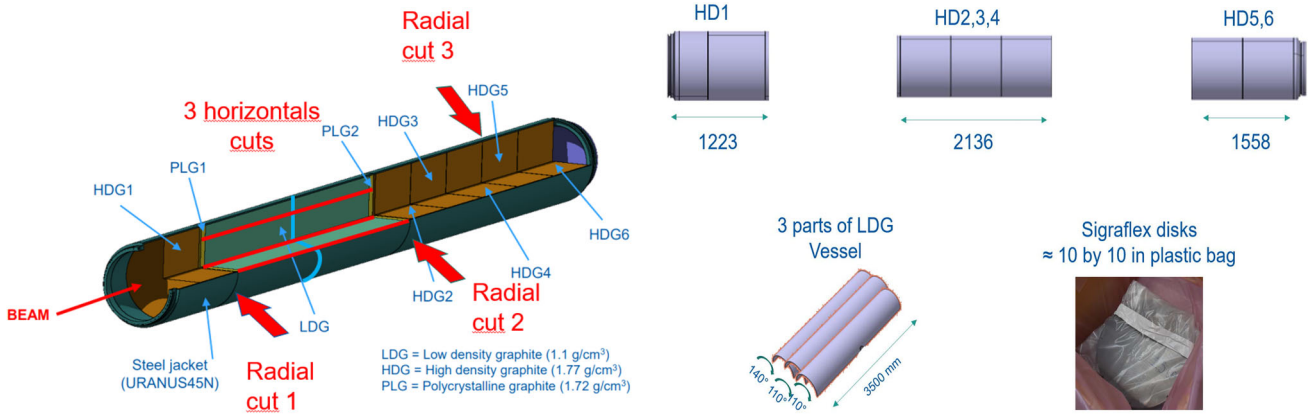


(a) Cuts performed on the TDE during the autopsy.

(b) Different TDE pieces to dispose as RW.

**Fig. 12** Process performed to fit the dump pieces inside the 10 $m^3$ container

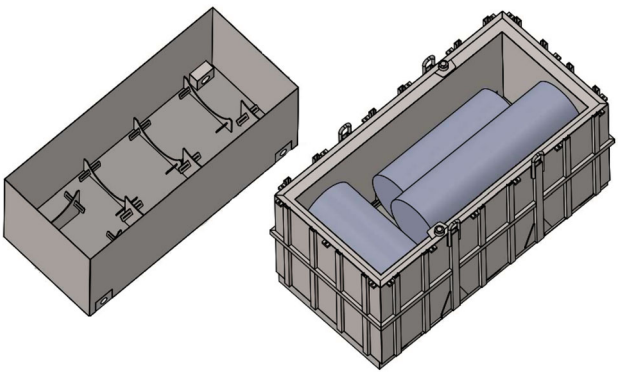

**Fig. 13** Left: lost mold. Right: the final container with three high-density graphite blocks inside

Finally all items shall fit inside the container. The TDE autopsy was conducted firstly by performing three radial cuts to split the dump into four main parts: HDG1, LDG, HDG2,3,4 and HDG5,6. Secondly, three horizontal cuts along the length of the LDG section were performed to extract the LDG disks, split them up in batches of 10 units to avoid the H-3 activity exceeding 50 GBq (see in Sect. 3) and isolate the LDG vessel in three independent parts (Fig. 12b). The three parts of the LDG vessel are treated separately as metallic FMA waste candidates for another elimination pathway.

The three blocks of HDG were placed inside a "lost mold" into which they fit perfectly and can be stowed safely. This "lost mold" is present inside the injectable container of 10 $m^3$ and 150 mm pre-concrete lining. Based on combined values in Table 3, the total tritium activity present inside the container is 19.7 GBq. This configuration allows to add LDG disks into the container, in batches of 10 units, until the limit of 50 GBq/container is reached. The filled container Fig. 13 will be shipped to the CSA following the transport rules described in Sect. 4 and it will be filled with mortar at the CSA before being disposed in an concrete-filled vault.

## 6 Conclusions

The present paper summarizes the radiological characterization of the LHC beam dump core (TDE), following the in-house TDE autopsy conducted in February 2022, in anticipation of the disposal of the dump as radioactive waste. Performing these activities in tandem had a number of benefits, including the requirement for only one worksite and minimizing staff radiation exposure. Radioactivity levels were estimated using a combination of Monte Carlo simulations (FLUKA) and analytical radionuclide inventory estimation software (ActiWiz). The main limiting nuclide (in terms of the various limits imposed by waste repositories) was found to be H-3 within the graphite core of the dump. Based on these findings, and aided by radiochemical analysis of samples of graphite, we determined that the TDE should be classed as medium-level (FMA-VC) waste, with the additional requirement that the waste is encapsulated in a concrete matrix. The dump will be stored in 10 $m^3$ injectable containers with 150 mm of pre-concreting. No major internal or external transport obstacles were identified.

Finally, it is important to note that the results presented here are related to a single LHC beam dump. This study created the in-house expertise necessary to dispose the second TDE removed during LS2, as well as the presently installed TDE which will be uninstalled at the end of Run 3, leaving room for a new generation of dumps capable of coping with HL-LHC beam intensity.

Furthermore, the expertise developed during the TDE autopsy/characterization may be employed to other highly activated equipment at CERN, for which the disposal as TFA might be not feasible.

**Acknowledgements** The authors would like also to thanks the CERN FLUKA team for sharing the original FLUKA model of the TDE core and for the very useful technical discussions and interactions.

**Funding** Open access funding provided by CERN (European Organization for Nuclear Research).

**Data Availability Statement** This manuscript has associated data in a data repository. [Authors' comment: The data that support the findings of this study are included in this publication. The full dataset is available from the corresponding author, on reasonable request evaluated case-by-case.]



## References

1. O.S. Brüning, P. Collier, P. Lebrun, S. Myers, R. Ostojic, J. Poole, P. Proudlock. LHC Design Report. CERN Yellow Reports: Monographs. CERN, Geneva (2004)
2. J. Maestre, C. Torregrosa, K. Kershaw, C. Bracco, T. Coiffet, M. Ferrari, R. Franqueira Ximenes, S. Gilardoni, D. Grenier, A. Lechner, V. Maire, J.M. Martin Ruiz, E. Matheson, N. Solieri, A. Perillo-Marcone, T. Polzin, V. Rizzoglio, D. Senajova, C. Sharp, M. Timmins, and M. Calviani. Design and behaviour of the large hadron collider external beam dumps capable of receiving 539 mj/dump. J. Instrum. **16**(11), P11019 (2021)
3. O. Aberle, I Béjar Alonso, O Brüning, P Fessia, L Rossi, L Tavian, M Zerlauth, C. Adorisio, A. Adraktas, M. Ady, J. Albertone, L. Alberty, M. Alcaide Leon, A. Alekou, D. Alesini, B. Almeida Ferreira, P. Alvarez Lopez, G. Ambrosio, P. Andreu Munoz, M. Anerella, D. Angal-Kalinin, F. Antoniou, G. Apollinari, A. Apollonio, R. Appleby, G. Arduini, B. Arias Alonso, K. Artoos, S. Atieh, B. Auchmann, V. Badin, T. Baer, D. Baffari, V. Baglin, M. Bajko, A. Ball, A. Ballarino, S. Bally, T. Bampton, D. Banfi, R. Barlow, M. Barnes, J. Barranco, L. Barthelemy, W. Bartmann, H. Bartosik, E. Barzi, M. Battistin, P. Baudrenghien, I. Bejar Alonso, S. Belomestnykh, A. Benoit, I. Ben-Zvi, A. Bertarelli, S. Bertolasi, C. Bertone, B. Bertran, P. Bestmann, N. Biancacci, A. Bignami, N. Bliss, C. Boccard, Y. Body, J. Borburgh, B. Bordini, F. Borralho, R. Bossert, L. Bottura, A. Boucherie, R. Bozzi, C. Bracco, E. Bravin, G. Bregliozzi, D. Brett, A. Broche, K. Brodzinski, F. Broggi, R. Bruce, M. Brugger, O. Brüning, X. Buffat, H. Burkhardt, J. Burnet, A. Burov, G. Burt, R. Cabezas, Y. Cai, R. Calaga, S. Calatroni, O. Capatina, T. Capelli, P. Cardon, E. Carlier, F. Carra, A. Carvalho, L.R. Carver, F. Caspers, G. Cattenoz, F. Cerutti, A. Chancé, M. Chastre Rodrigues, S. Chemli, D. Cheng, P. Chiggiato, G. Chlachidze, S. Claudet, JM. Coello De Portugal, C. Collazos, J. Corso, S. Costa Machado, P. Costa Pinto, E. Coulinge, M. Crouch, P. Cruikshank, E. Cruz Alaniz, M. Czech, K. Dahlerup-Petersen, B. Dalena, G. Daniluk, S. Danzeca, H. Day, J. De Carvalho Saraiva, D. De Luca, R. De Maria, G. De Rijk, S. De Silva, B. Dehning, J. Delayen, Q. Deliege, B. Delille, F. Delsaux, R. Denz, A. Devred, A. Dexter, B. Di Girolamo, D. Dietderich, J.W. Dilly, A. Doherty, N. Dos Santos, A. Drago, D.Drskovic, D. Duarte Ramos, L. Ducimetière, I. Efthymiopoulos, K. Einsweiler, L. Esposito, J. Esteban Muller, S. Evrard, P. Fabbricatore, S. Farinon, S. Fartoukh, A. Faus-Golfe, G. Favre, H. Felice, B. Feral, G. Ferlin, P. Ferracin, A. Ferrari, L. Ferreira, P. Fessia, L. Ficcadenti, S. Fiotakis, L. Fiscarelli, M. Fitterer, J. Fleiter, G. Foffano, E. Fol, R. Folch, K. Foraz, A. Foussat, M. Frankl, O. Frasciello, M. Fraser, P. Freijedo Menendez, J-F. Fuchs, S. Furuseth, A. Gaddi, M. Gallilee, A. Gallo, R. Garcia Alia, H. Garcia Gavela, J. Garcia Matos, H. Garcia Morales, A. Garcia-Tabares Valdivieso, C. Garino, C. Garion, J. Gascon, Ch. Gasnier, L. Gentini, C. Gentsos, A. Ghosh, L. Giacomel, K. Gibran Hernandez, S. Gibson, C. Ginburg, F. Giordano, M. Giovannozzi, B. Goddard, P. Gomes, M. Gonzalez De La Aleja Cabana, P. Goudket, E. Gousiou, P. Gradassi, A. Granadeiro Costa, L. Grand-Clément, S. Grillot, JC. Guillaume, M. Guinchard, P. Hagen, T. Hakulinen, B. Hall, J. Hansen, N. Heredia Garcia, W. Herr, A. Herty, C. Hill, M. Hofer, W. Höfle, B. Holzer, S. Hopkins, J. Hrivnak, G. Iadarola, A. Infantino, S. Izquierdo Bermudez, S. Jakobsen, M.A. Jebramcik, B. Jenninger, E. Jensen, M. Jones, R. Jones, T. Jones, J. Jowett, M. Juchno, C. Julie, T. Junginger, V. Kain, D. Kaltchev, N. Karastathis, P. Kardasopoulos, M. Karppinen, J. Keintzel, R. Kersevan, F. Killing, G. Kirby, M. Korostelev, N. Kos, S. Kostoglou, I. Kozsar, A. Krasnov, S. Krave, L. Krzempek, N. Kuder, A. Kurtulus, R. Kwee-Hinzmann, F. Lackner, M. Lamont, A.L. Lamure, L. Lari m, M. Lazzaroni, M. Le Garrec, A. Lechner, T. Lefevre, R. Leuxe, K. Li, Z. Li, R. Lindner, B. Lindstrom, C. Lingwood, C. Löffler, C. Lopez, LA. Lopez-Hernandez, R. Losito, F. Maciariello, P. Macintosh, E.H. Maclean, A. Macpherson, P. Maesen, C. Magnier, H. Mainaud Durand, L. Malina, M. Manfredi, F. Marcellini, M. Marchevsky, S. Maridor, G. Marinaro, K. Marinov, T. Markiewicz, A. Marsili, P. Martinez Urioz, M. Martino, A. Masi, T. Mastoridis, P. Mattelaer, A. May, J. Mazet, S. Mcilwraith, E. McIntosh, L. Medina Medrano, A. Mejica Rodriguez, M. Mendes, P. Menendez, M. Mensi, A. Mereghetti, D. Mergelkuhl, T. Mertens, L. Mether, E. Métral, M. Migliorati, A. Milanese, P. Minginette, D. Missiaen, T. Mitsuhashi, M. Modena, N. Mokhov, J. Molson, E. Monneret, E. Montesinos, R. Moron-Ballester, M. Morrone, A. Mostacci, N. Mounet, P. Moyret, P. Muffat, B. Muratori, Y. Muttoni, T. Nakamoto, M. Navarro-Tapia, H. Neupert, L. Nevay, T. Nicol, E. Nilsson, P. Ninin, A. Nobrega, C. Noels, E. Nolan, Y. Nosochkov, FX. Nuiry, L. Oberli, T. Ogitsu, K. Ohmi, Olave R., J. Oliveira, Ph. Orlandi, P. Ortega, J. Osborne, T. Otto, L. Palumbo, S. Papadopoulou, Y. Papaphilippou, K. Paraschou, C. Parente, S. Paret, H. Park, V. Parma, Ch. Pasquino, A. Patapenka, L. Patnaik, S. Pattalwar, J. Payet, G. Pechaud, D. Pellegrini, P. Pepinster, J. Perez, J. Perez Espinos, A. Perillo Marcone, A. Perin, P. Perini, T.H.B. Persson, T. Peterson, T. Pieloni, G. Pigny, J.P. Pinheiro de Sousa, O. Pirotte, F. Plassard, M. Pojer, L. Pontercorvo, A. Poyet, D. Prelipcean, H. Prin, R. Principe, T. Pugnat, J. Qiang, E. Quaranta, H. Rafique, I. Rakhno, D. Ramos Duarte, A. Ratti, E. Ravaioli, M. Raymond, S. Redaelli, T. Renaglia, D. Ricci, G. Riddone, J. Rifflet, E. Rigutto, T. Rijoff, R. Rinaldesi, O. Riu Martinez, L. Rivkin, F. Rodriguez Mateos, S. Roesler, I. Romera Ramirez, A. Rossi, L. Rossi, V. Rude, G. Rumolo, J. Rutkovksi, M. Sabate Gilarte, G. Sabbi, T. Sahner, R. Salemme, B. Salvant, F. Sanchez Galan, A. Santamaria Garcia, I. Santillana, C. Santini, O. Santos, P. Santos Diaz, K. Sasaki, F. Savary, A. Sbrizzi, M. Schaumann, C. Scheuerlein, J. Schmalzle, H. Schmickler, R. Schmidt, D. Schoerling, M. Segreti, M. Serluca, J. Serrano, J. Sestak, E. Shaposhnikova, D. Shatilov, A. Siemko, M. Sisti, M. Sitko, J. Skarita, E. Skordis, K. Skoufaris, G. Skripka, D. Smekens, Z. Sobiech, M. Sosin, M. Sorbio, F. Soubelet, B. Spataro, G. Spiezia, G. Stancari, M. Staterao, J. Steckert, G. Steele, G. Sterbini, M. Struik, M. Sugano, A. Szeberenyi, M. Taborelli, C. Tambasco, R. Tavares Rego, L. Tavian, B. Teissandier, N. Templeton, M. Therasse, H. Thiesen, E. Thomas, A. Toader, E. Todesco, R. Tomás, F. Toral, R. Torres-Sanchez, G. Trad, N. Triantafyllou, I. Tropin, A. Tsinganis, J. Tuckamantel, J. Uythoven, A. Valishev, F. Van Der Veken, R. Van Weelderen, A. Vande Craen, B. Vazquez De Prada, F. Velotti, S. Verdu Andres, A. Verweij, N. Vittal Shetty, V. Vlachoudis, G. Volpini, U. Wagner, P. Wanderer, M. Wang, X. Wang,

R. Wanzenberg, A. Wegscheider, S. Weisz, C. Welsch, M. Wendt, J. Wenninger, W. Weterings, S. White, K. Widuch, A. Will, G. Willering, D. Wollmann, A. Wolski, J. Wozniak, Q. Wu, B. Xiao, L. Xiao, Q. Xu, Y. Yakovlev, S. Yammine, Y. Yang, M. Yu, I. Zacharov, O. Zagorodnova, C. Zannini, C. Zanoni, M. Zerlauth, F. Zimmermann, A. Zlobin, M. Zobov, I. Zurbano Fernandez. High-Luminosity Large Hadron Collider (HL-LHC): technical design report. CERN Yellow Reports: Monographs. CERN, Geneva (2020)

4. A. Infantino, D. Björkman, L. Elie, M. Maietta, C. Tromel, H. Vincke, Radiation protection at the large hadron collider: problematics, challenges and advanced Monte Carlo simulation techniques. Environments **9**(5), 54 (2022)
5. A. Infantino, A.P. Bernardes, M. Calviani, G. Dumont, S. El-Idrissi, R. Mouret, C. Tromel, H. Vincke, Radiation protection challenges in the upgrade, autopsy and disposal of the LHC beam dump. Radiat. Protect. Dosimet. **199**(8–9), 891–899 (2023)
6. CERN. FLUKA CERN website (2020). Available online: https://fluka.cern (online). Accessed 11 Apr 2023
7. C. Ahdida, D. Bozzato, D. Calzolari, F. Cerutti, N. Charitonidis, A. Cimmino, A. Coronetti, G.L. D'Alessandro, A. Donadon Servelle, L.S. Esposito, R. Froeschl, R. García Alía, A. Gerbershagen, S. Gilardoni, D. Horváth, G. Hugo, A. Infantino, V. Kouskoura, A. Lechner, B. Lefebvre, G. Lerner, M. Magistris, A. Manousos, G. Moryc, F. Ogallar Ruiz, F. Pozzi, D. Prelipcean, S. Roesler, R. Rossi, M. Sabaté Gilarte, F. Salvat Pujol, P. Schoofs, V. Stránský, C. Theis, A. Tsinganis, R. Versaci, V. Vlachoudis, A. Waets, M. Widorski. New capabilities of the FLUKA multi-purpose code. Front. Phys. **9**, 788253 (2022)
8. G. Battistoni, T. Boehlen, F. Cerutti, P.W. Chin, L.S. Esposito, A. Fassò, A. Ferrari, A. Lechner, A. Empl, A. Mairani, A. Mereghetti, P. Garcia Ortega, J. Ranft, S. Roesler, P.R. Sala, V. Vlachoudis, G. Smirnov. Overview of the FLUKA code. Ann. Nucl. Energy **82**, 10–18 (2015)
9. H. Vincke, C. Theis. Actiwiz 3—an overview of the latest developments and their application. J. Phys.: Confer. Ser. **1046**(1), 012007 (2018)
10. T. Oyama, T. Sanami, H. Yashima, M. Hagiwara, N. Nakao, A. Infantino, E. Iliopoulou, R. Froeschl, S. Roesler, T. Kajimoto, E. Lee, S. Nagaguro, T. Matsumoto, A. Masuda, Y. Uwamino, Measurements of secondary-particle emissions from copper target bombarded with 24-GeV/c protons. Nucl. Instrum. Methods Phys. Res., Sect. A **990**, 164977 (2021)
11. C. Ahdida, R. Froeschl, E. Iliopoulou, A. Infantino, S. Jensen, Measurements and fluka simulations of aluminium, bismuth and indium activation by stray radiation from the annihilation of low energy antiprotons. Nucl. Instrum. Methods Phys. Res., Sect. A **950**, 162972 (2020)
12. T. Oyama, M. Hagiwara, T. Sanami, H. Yashima, N. Nakao, E.J. Lee, E. Iliopoulou, R. Froeschl, A. Infantino, S. Roesler, Measurement and calculation of thermal neutrons induced by the 24 GeV/c proton bombardment of a thick copper target. Nucl. Instrum. Methods Phys. Res., Sect. B **434**, 29–36 (2018)
13. E. Iliopoulou, P. Bamidis, M. Brugger, R. Froeschl, A. Infantino, T. Kajimoto, N. Nakao, S. Roesler, T. Sanami, A. Siountas, Measurements and fluka simulations of bismuth and aluminium activation at the CERN shielding benchmark facility (csbf). Nucl. Instrum. Methods Phys. Res., Sect. A **885**, 79–85 (2018)
14. International Atomic Energy Agency (IAEA), *Characterization, Treatment and Conditioning of Radioactive Graphite from Decommissioning of Nuclear Reactors. Number 1521 in TECDOC Series* (Vienna, 2006)
15. International Atomic Energy Agency (IAEA), *Progress in Radioactive Graphite Waste Management, Number 1647 in TECDOC Series* (Vienna, 2010)
16. International Atomic Energy Agency (IAEA), *Processing of Irradiated Graphite to Meet Acceptance Criteria for Waste Disposal. Number 1790 in TECDOC Series* (Vienna, 2016)
17. J. Wozniak, C. Roderick. NXCALS—architecture and challenges of the next CERN accelerator logging service, in *17th Biennial International Conference on Accelerator and Large Experimental Physics Control Systems (ICALEPCS), New York, USA, 5–11 Oct 2019* (2020), p. WEPHA163
18. R. Froeschl, A method for radiological characterization based on fluence conversion coefficients. J. Phys.: Confer. Ser. **1046**(1), 012006 (2018)
19. ANDRA. Spécification d'Acceptation des colis de déchets radioactifs au CSFMA (INB No 149), Spécification d'évaluation et de déclaration des caractéristiques radioactives 2014. Available online: https://docplayer.fr/87439106-Specification-d-acceptation-des-colis-de-dechets-radioactifs-au-csfma-inb-n-149.html (online). Accessed 11 Apr 2023
20. United Nations, Economic Commission for Europe. Agreement concerning the International Carriage of Dangerous Goods by Road (2023)